The first steps of planet formation : studying grain growth with millimetre interferometers

Lommen, D.J.P.

Chapter 3

Investigating grain growth in discs around southern T-Tauri stars at millimetre wavelengths

Abstract

Low-mass stars form with discs in which the coagulation of grains may eventually lead to the formation of planets. It is not known when and where grain growth occurs, as models that explain the observations are often degenerate. A way to break this degeneracy is to resolve the sources under study. We here aim to find evidence for the existence of grains of millimetre sizes in discs around in T-Tauri stars, implying grain growth. The Australia Telescope Compact Array (ATCA) was used to observe 15 southern T-Tauri stars, five in the constellation Lupus and ten in Chamaeleon, at 3.3 millimetre. The five Lupus sources were also observed with the Submillimeter Array (SMA) at 1.4 millimetre. Our new data are complemented with data from the literature to determine the slopes of the spectral energy distributions in the millimetre regime. Ten sources were detected at better than 3σ with the ATCA, with $\sigma \approx 1$–2 mJy, and all sources that were observed with the SMA were detected at better than 15σ, with $\sigma \approx 4$ mJy. Six of the sources in our sample are resolved to physical radii of $\sim$ 100 AU. Assuming that the emission from such large discs is predominantly optically thin, the millimetre slope can be related directly to the opacity index. For the other sources, the opacity indices are lower limits. Four out of six resolved sources have opacity indices $\lesssim 1$, indicating grain growth to millimetre sizes and larger. The masses of the discs range from < 0.01 to 0.08 $M_\odot$, which is comparable to the minimum mass solar nebula. A tentative correlation is found between the millimetre slope and the strength and shape of the 10-μm silicate feature, indicating that grain growth occurs on similar (short) timescales in both the inner and outer disc.

Dave Lommen, Chris Wright, Sarah Maddison, Jes Jørgensen,
Tyler Bourke, Ewine van Dishoeck, Annie Hughes, David Wilner,
Michael Burton, and Huib Jan van Langevelde

Astronomy & Astrophysics 2007, 462, 211

3.1 Introduction

Discs of dust and gas are observed around many young stars. According to the so-called core-accretion model (Safronov & Zvjagina 1969), planetary systems such as our own Solar System are formed in these circumstellar discs: the solid particles coagulate to form larger grains, which will grow to eventually form planets. The grains mainly consist of carbon and silicates. The silicate grains are readily observed through their 10- and 20-μm features. Both the change from amorphous to more crystalline grains, as well as the growth of grains from submicron sizes to sizes of several μm have been observed by the Infrared Space Observatory (ISO, Malfait et al. 1998; van Boekel et al. 2005), and more recently by the Spitzer Space Telescope (Kessler-Silacci et al. 2006). Although the qualitative picture of grain growth has become much clearer over the last few years, several quantitative details are still under discussion. Open questions include for example the timescale over which grain growth occurs and how this relates to the disc's physical structure (e.g., its temperature and density profile). See Dominik et al. (2006) for a recent discussion of both laboratory measurements and theoretical modelling of the aggregation of dust in protoplanetary discs.

A large sample of solar-mass T-Tauri stars have recently been observed with the InfraRed Spectrograph (IRS) on board the Spitzer Space Telescope, in the context of the "Cores to Disks" (c2d) legacy (Evans et al. 2003) and other programmes. Most of the sources in the c2d sample show 10- and 20-μm amorphous silicate features (Kessler-Silacci et al. 2006), confirming the results of earlier ISO and ground-based 10-μm observations (e.g., van Boekel et al. 2003; Przygodda et al. 2003), and extending the observed protoplanetary disc sample to lower mass objects. The data indicate a large variety of silicate profiles, ranging from strongly peaked silicate bands and steeply rising spectral energy distributions (SEDs) to "boxy" silicate profiles and flat SEDs. The boxy features with low feature-to-continuum ratios are interpreted as grain growth to micron size (Bouwman et al. 2001).

One possible explanation for the different spectra and SEDs is that grain growth and the shape of the disc are related. Dullemond & Dominik (2004a) identified a correspondence between the growth of grains in a circumstellar disc and the evolution of the disc from a "flaring" to a "self-shadowed" geometry. In their models, the larger, more massive dust grains settle to the midplane of the discs as the grains grow, and the initially flared discs evolve into flatter, self-shadowed discs. To what extent this process is related to the age of the young star is still under debate; there are indications that some young stellar objects evolve more quickly than others.

Numerical models show that the process of settling and coagulation is rapid, being well underway at distances of 1–30 AU from the central star in $\sim 10^4$ yrs (e.g., Nomura & Nakagawa 2006). Models predict that the slopes of the SEDs in the millimetre wavelength range will become shallower as the grains in the disc grow to millimetre (mm) and subsequently centimetre (cm) and larger sizes (Dullemond & Dominik 2004a; D'Alessio et al. 2006). It is therefore necessary to observe these sources at larger wavelengths than the infrared. Furthermore, millimetre observations probe the entire disc, including the cold midplane, whereas infrared observations can only probe the hot surface layer of the inner disc. However, a shallow millimetre slope in itself is not enough evidence for grain growth in the discs, since an excess flux at long wavelengths may also be caused by a very small, optically thick disc (see, e.g., Beckwith & Sargent 1991). To break this degeneracy it is necessary to resolve the discs to determine their actual sizes, since if the physical disc size is known, a reasonable estimate of the disc's opacity can be obtained. To resolve the discs around T-Tauri stars, interferometric observations are indispensable.

Considerable progress has been made in this field over the last several years. Wilner et al. (2000) resolved the inner disc of the classical T-Tauri star TW Hya in dust emission at 7 mm using the Very Large Array (VLA). Calvet et al. (2002) did extensive modelling of the SED of this source and showed that the dust grains in the disc must have grown to sizes of at least $\sim$ 1 cm. Wilner et al. (2003) used the Australia Telescope Compact Array (ATCA) to study TW Hya at 3.4 mm and found that a passive two-layer disc (Chiang & Goldreich 1999) provides a reasonable model to explain the observations. Ten T-Tauri stars in the Taurus-Auriga star-forming regions were resolved at 7 mm with the VLA by Rodmann et al. (2006); the majority of these show strong evidence for grain growth to at least millimetre-sized dust.

The more massive counterparts of the T-Tauri stars, the Herbig-Ae/Be stars, have been studied extensively. Meeus et al. (2001) classified 14 isolated Herbig-Ae/Be stars into two groups based on the shape of the SED. Discs with a flared outer part of the disc show a rising mid-infrared (20–100 μm) excess (*Group I* in the classification by Meeus et al. 2001), whereas self-shadowed discs have more modest mid-infrared excesses (*Group II*). Acke et al. (2004) compared the millimetre slopes for a sample of 26 Herbig-Ae/Be stars, based on single-dish data, and found that *Group II* sources have in general a shallower slope, consistent with grain growth to larger sizes than in the *Group I* sources, and observationally confirming the model predictions from Dullemond & Dominik (2004a). Natta et al. (2004) analysed interferometric observations of nine pre-main-sequence

stars, mostly Herbig-Ae stars, and find that the observations are well explained with dust size distributions containing boulders of up to metre sizes.

We have used the ATCA to observe 3.3 mm continuum emission from a sample of 15 southern T-Tauri stars, five in Lupus and ten in Chamaeleon. Compared with the Taurus star-forming cloud, the T-Tauri stars in Lupus and Chamaeleon are generally somewhat older, and the Lupus clouds are much richer in very low mass stars than the other clouds (Hughes et al. 1994). The sources IM Lup and WW Cha were also observed in spectral-line mode to search for HCO^+ as a tracer of the molecular gas. The observations of the Lupus sources were followed up with 1.4-mm observations using the Submillimeter Array (SMA). The sample and the observations are described in Sect. 3.2. The basic results are presented in Sect. 3.3 and further discussed in Sect. 3.4. We will summarise our results and draw some conclusions in Sect. 3.5.

3.2 Observations

3.2.1 Source selection

The ATCA was used to observe 15 southern T-Tauri stars (listed in Table 3.1) at 3.3 mm. The sources were selected to overlap with the sample observed in the c2d programme. We furthermore selected sources with strong 1.3 mm fluxes (Henning et al. 1993; Nürnberger et al. 1997) to improve the chances of detection at 3.3 mm.

The distances used in this work are 150 ± 20 pc to Lupus I (HT Lup, GW Lup) and Lupus II (IM Lup, RU Lup), 200 ± 20 pc to Lupus III (HK Lup) (Comerón 2008), and 160 ± 15 pc to Chamaeleon I (Whittet et al. 1997). The distances to most of these pre-main-sequence stars are not very well constrained (see, e.g., Comerón 2008; van Kempen et al. 2007, for discussions on the distances to the Lupus clouds). The distance to the isolated source T Cha, however, is known to be closer at 66^{+19}_{-12} pc (Hipparcos, van den Ancker et al. 1998).

3.2.2 ATCA observations

ATCA[1] observations were carried out in July 2003, October 2004, and August 2005. All sources were observed at 3.3 mm continuum in double sideband. The primary beam of the ATCA antennas is $\approx 35''$ at 3 mm. Each sideband consisted

[1]The Australia Telescope Compact Array is part of the Australia Telescope which is funded by the Commonwealth of Australia for operation as a National Facility managed by CSIRO.

of 32 channels and had an effective total bandwidth of 128 MHz. Furthermore, the sources WW Cha and IM Lup were observed in a dual mode: the lower sideband was a 512-channel band with an effective total bandwidth of 8 MHz to provide high-frequency resolution for detection of the HCO^+ J = 1–0 line and the upper sideband was used as a wideband channel with again 32 channels and a total bandwidth of 128 MHz. These two sources were observed for a complete track to reach a similar RMS noise in the continuum as that for the other sources, and to maximise the possibility of detecting the HCO^+ J = 1–0 line. The resulting velocity resolution of the narrow-band observations was 0.11 km s^{-1}, the velocity coverage was ∼24 km s^{-1}. The ATCA was in the EW214 configuration at the time of the observations in 2003 (three antennas equipped with 3 mm receivers, baselines of 31–107 metres) and in the H214C configuration in 2004 and 2005 (five antennas, baselines of 82–247 metres). The data were calibrated and reduced with the MIRIAD package (Sault et al. 1995). The quasars PKS 1622-297 and PKS 1057-797 served as gain calibrators for the Lupus and Chamaeleon sources, respectively, and the absolute fluxes were calibrated on Mars or Uranus. The calibration is estimated to have an uncertainty of ∼20 %. The passbands were calibrated on the quasars PKS 0537-441 and PKS 1253-055.

The phase centre was offset from the source position by 5″ to avoid possible artefacts. There was some overlap in the samples that were observed in the three runs. The 2004 data suffered badly from unstable weather and were not used in the analysis, whereas the 2003 and 2005 data were consistent. In 2003, there were only three ATCA antennas fitted with 3 mm receivers, resulting in a large and elongated beam. Five antennas with 3 mm receivers were available in 2005, greatly improving the resolution and beam shape of our observations. With the exception of HK Lup, which was only observed in 2003, we decided to use only the 2005 data for our analysis. For an overview of the ATCA observations, see Table 3.2.

3.2.3 SMA observations

The five Lupus sources in our sample were observed in double-sideband continuum (217 and 227 GHz, primary beam ∼ 55″) with the SMA[2] (Ho et al. 2004) on 28 April 2006. The data from both sidebands were combined, giving an effective bandwidth of 3 GHz. The SMA was in the compact configuration and baselines ranged from 5 to 52 metres. The low elevation of the sources as seen from Mauna

[2]The Submillimeter Array is a joint project between the Smithsonian Astrophysical Observatory and the Academia Sinica Institute of Astronomy and Astrophysics and is funded by the Smithsonian Institution and the Academia Sinica.

Table 3.1: Source list of sources observed with the ATCA.

Source	Cloud	Age[a] (Myr)	Spectral type[b]	L[c] ($L_\odot$)	D[d] (pc)	When observed[e]
SY Cha	Cha I	3–5	M0	0.35	160 ± 15	2005
CR Cha	Cha I	1–2	K0, K2	2.8	160 ± 15	2003†; 2005
CS Cha	Cha I	2–3	K4	1.3	160 ± 15	2003†; 2005
DI Cha	Cha I	3–4	G1, G2	8.9	160 ± 15	2005
KG 28	Cha I	...	K7	1.1	160 ± 15	2005
Glass I[f]	Cha I	2–3	K4	1.3	160 ± 15	2005
KG 49	Cha I	...	...	15	160 ± 15	2005
WW Cha	Cha I	0.4–0.8	K5	2.2	160 ± 15	2003†; 2005
XX Cha	Cha I	10–40	M1	0.10	160 ± 15	2005
T Cha	Isolated	> 12.5	G2	1.3	66^{+19}_{-12}	2003†; 2005
HT Lup[g]	Lup I	0.4–0.8	K2	6.0	150 ± 20	2003†; 2005
GW Lup	Lup I	1.3–3.2	M2	0.23	150 ± 20	2003†; 2005
IM Lup	Lup II	0.09–0.6	M0	1.3	150 ± 20	2003†; 2005
RU Lup	Lup II	0.04–0.5	K7-M0	2.1	150 ± 20	2003†; 2005
HK Lup	Lup III	0.7–1.4	M0	0.62	200 ± 20	2003

[a] Ages adopted from Hughes et al. (1994), Lawson et al. (1996), and van den Ancker et al. (1998).

[b] Spectral types adopted from Herbig & Kameswara Rao (1972), Gauvin & Strom (1992), Hughes et al. (1994), Alcala et al. (1995), van den Ancker et al. (1998), and Comerón et al. (1999).

[c] Luminosities adopted from Hughes et al. (1994), Lawson et al. (1996), Chen et al. (1997), and van den Ancker et al. (1998).

[d] Distances adopted from Whittet et al. (1997), van den Ancker et al. (1998), and Comerón (2008).

[e] The observations marked with a † were not used in the analysis.

[f] This source is a binary with a separation of 2.″4; the spectrum quoted is that of component A.

[g] This source is a binary in 2MASS K-band images with a separation < 3″. The spectrum quoted includes both sources.

Table 3.2: Overview of the observations.

Obs. dates	Freqs. covered (GHz)	(u, v) range covered (kλ)	# Antennas used
	ATCA		
10 July 2003	89.999, 90.095	8-33	3
11 July 2003	89.999, 90.095	9-33	3
12 July 2003	89.999, 90.095	6-33	3
13 July 2003	89.999, 90.095	6-33	3
19 August 2005	89.181, 91.456	19-76	5
24 August 2005	89.180, 91.456	12-70	5
	90.000, 90.096	14-75	5
25 August 2005	89.176, 91.456	10-71	5
26 August 2005	89.176, 91.456	12-71	5
28 August 2005	89.176, 91.456	12-71	5
	SMA		
28 April 2006	217.347, 226.892	4-53	8

Kea and the relatively short integration time of $\sim$ 30 minutes per source resulted in a rather elongated beam of $\sim 9 \times 2.5$ arcsec (natural weighting). The raw visibility data were calibrated and flagged with MIR, and the calibrated visibility data were analysed with MIRIAD. The gains were calibrated on the quasar PKS 1622-297, and the absolute fluxes and correlator passbands were calibrated on Uranus with an expected uncertainty of ~20 %. All eight antennas of the array were available at the time of the observations. For an overview of the SMA observations, see Table 3.2.

3.3 Results

3.3.1 Source fluxes

From the 15 sources that were observed with the ATCA in 2003 and 2005, ten were detected at better than 3σ, with 3.3 mm fluxes ranging from $\sim$ 6 mJy up to $\sim$ 30 mJy. For those objects, both point sources and circular Gaussians were fitted in the (u, v) plane, the results of which are presented in Table 3.3. Those sources that were detected at better than 5σ are shown in Fig. 3.1, overplotted on 2MASS K-band (2.1 μm) images. The positions of the infrared sources and the millimetre peaks agree very well.

Table 3.3: Basic results of ATCA observations at 3.3 mm.

Source name	Continuum flux[a] (mJy)		RMS[b] (mJy/beam)	Gaussian size (arcsec)	RA[a] (J2000)	Dec.[a] (J2000)	Beam size[c] (arcsec)	$\nu_{\rm eff}$ (GHz)
	(P)	(G)						
SY Cha	< 4.8[d]		1.6	-	10 56 30.4	-77 11 45.0	2.5×2.2	90.3
CR Cha	6.2	6.1	1.5	< 1	10 59 06.9	-77 01 39.7	2.5×2.1	90.3
CS Cha	5.9	8.8	1.5	1.65 ± 0.96	11 02 24.9	-77 33 35.9	2.4×2.2	90.3
DI Cha	< 3.9[d]		1.3	-	11 07 21.6	-77 38 12.0	2.4×2.2	90.3
KG 28	< 3.9[d]		1.3	-	11 07 57.9	-77 38 50.0	2.4×2.3	90.3
Glass I	< 3.0[d]		1.0	-	11 08 15.1	-77 33 59.0	2.4×2.4	90.3
KG 49	11.9	29.5	1.5	2.78 ± 0.40	11 08 38.6	-77 43 52.1	2.4×2.2	90.3
WW Cha	25.9	33.1	1.2	1.32 ± 0.16	11 10 00.0	-76 34 58.0	2.5×2.2	91.0
XX Cha	< 4.5[d]		1.5	-	11 11 39.7	-76 20 21.0	2.4×2.2	90.3
T Cha	6.4	7.0	1.0	0.78 ± 1.03	11 57 13.6	-79 21 31.7	2.5×2.4	90.3
HT Lup	8.3	12.0	1.1	1.40 ± 0.41	15 45 12.9	-34 17 30.8	2.4×1.7	90.0
GW Lup	8.5	9.5	1.9	0.98 ± 1.22	15 46 44.7	-34 30 36.0	5.3×1.7	90.0
IM Lup	8.9	13.1	1.3	1.40 ± 0.39	15 56 09.2	-37 56 06.3	2.3×1.7	91.5
RU Lup	12.7	15.6	1.0	0.99 ± 0.32	15 56 42.3	-37 49 16.0	2.3×1.7	90.0
HK Lup	7.3	9.1	2.1	2.85 ± 1.70	16 08 22.5	-39 04 46.3	ill defined[e]	90.1

NOTE. — Source name in boldface indicates that the source is resolved at 3.3 mm with the ATCA, see Sect. 3.3.2.

[a] Continuum flux and position are from fits in the (u, v) plane. For sources that were detected at 3σ, both the point-source flux (P) and the integrated flux for a Gaussian (G) are shown. For sources that were not detected, the coordinates of the phase centre are quoted.

[b] Calculated from the cleaned image.

[c] Restored beam, using natural weighting.

[d] Quoted value is 3σ upper limit.

[e] Large, elongated beam due to short integration time and availability of only three antennas with 3 mm receivers.

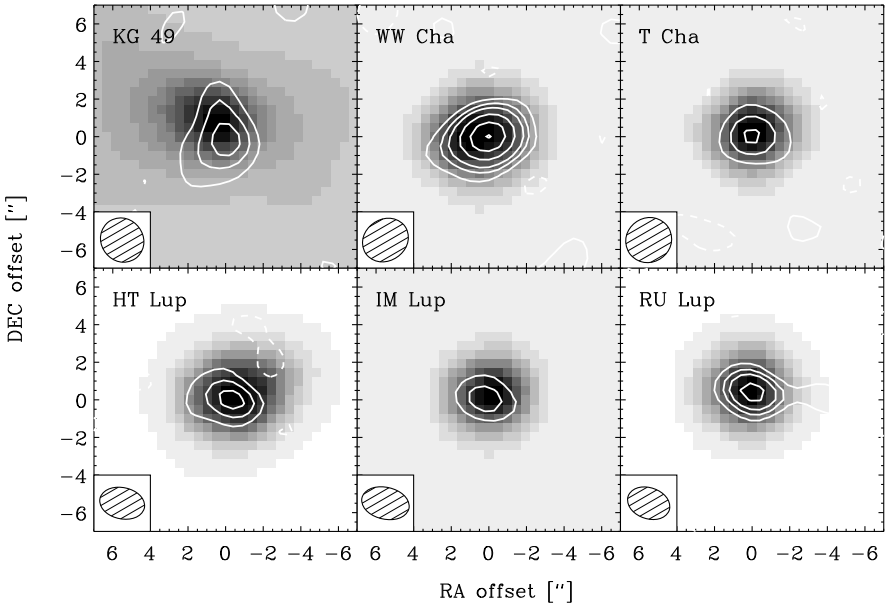

Figure 3.1: ATCA images of the $\lambda = 3.3$-mm continuum emission (contours), overplotted on 2MASS K-band (2.1 μm) images (grayscales). Contour levels are drawn at 2, 4, 6, 10, 15, and 20 times the noise level; negative contours are dashed. The positional offsets are with respect to the fitted coordinates (see Table 3.3).

Table 3.4 presents the results of the SMA 1.4-mm observations of the Lupus sources, which were all detected at better than 15σ, with fluxes ranging from $\sim$ 70 mJy up to $\sim$ 210 mJy. For comparison, the SEST 1.3 mm single-dish fluxes from Nürnberger et al. (1997) are also shown.

3.3.2 Are the sources resolved?

A plot of the visibility amplitude as a function of baseline for each of our target sources is presented in Figs. 3.2 and 3.3. An amplitude that decreases as a function of baseline indicates a resolved source, suggesting that at least some of our sources are resolved. Note that in principle the resolved structure could be the protoplanetary disc, or the remnant centrally-condensed envelope around it. One can distinguish between the two by looking in more detail at the shape of the

Table 3.4: Basic results of SMA observations at 1.4 mm. For comparison, the SEST 1.3 mm single-dish fluxes from Nürnberger et al. (1997) are shown.

Source name	Continuum flux[a] (mJy)		RMS[b] (mJy/beam)	Gaussian size (arcsec)	RA[a] (J2000)	Dec.[a] (J2000)	$\nu_{\rm eff}$ (GHz)	SEST 1.3 mm[c]	
	(P)	(G)						Flux (mJy)	RMS (mJy)
HT Lup	73	77	4.0	1.01 ± 0.66	15 45 12.9	-34 17 30.1	221.3	135	15
GW Lup	64	70	3.7	1.22 ± 0.48	15 46 44.8	-34 30 35.7	221.3	106	18
IM Lup	188	214	4.3	1.33 ± 0.20	15 56 09.2	-37 56 06.5	221.3	260	9
RU Lup	148	158	4.5	1.02 ± 0.32	15 56 42.3	-37 49 15.9	221.3	197	7
HK Lup	89	101	3.9	1.43 ± 0.38	16 08 22.5	-39 04 47.5	221.3	84	17

NOTE. — Source name in boldface indicates that the source is resolved at 1.4 mm with the SMA, see Sect. 3.3.2.

[a] Continuum flux and position are taken from fits in the (u, v) plane. Both the point-source flux (P) and the integrated flux for a Gaussian (G) are shown.

[b] Calculated from the cleaned image.

[c] Nürnberger et al. (1997). The SEST fluxes are in general higher than the SMA fluxes, partly due to the slightly shorter effective wavelength, 1.3 mm (SEST) vs 1.4 mm (SMA).

amplitude vs (u, v) distance curves. A disc shows a shallower profile at shorter baselines, levelling off to the flux of the integrated disc emission. A power-law envelope shows a flux that increases steeply towards the shortest baselines, and the total integrated flux can only be obtained with single-dish telescopes, observing with a larger beam. An illustrative example is provided by Fig. 3 in Jørgensen et al. (2005), who need a disc and an envelope to explain the amplitude as a function of baseline for the deeply embedded class 0 source NGC 1333 IRAS 2A.

The amplitude vs (u, v) distance plot for KG 49 (Cha IRN) appears to indicate a resolved envelope rather than a disc. This is in line with the results of Henning et al. (1993) who find that the SED from 1 μm to 1 mm cannot be fitted with a disc, but is consistent with a spherically symmetric model with constant density and $A_V = 25$ mag. Furthermore, all other sources show silicates in emission around 10 μm, which is indicative of a disc without significant foreground absorption. KG 49 on the other hand does not show silicate emission around 10 μm. However, it does show bands of H_2O, CO, and CO_2 ice (Gürtler et al. 1999; Pontoppidan et al. 2003), which can be explained by a cold envelope. It thus appears that KG 49 is not a genuine T-Tauri star, but a less evolved object that is still embedded in an envelope. We will therefore disregard KG 49 in the further analysis in this work.

We consider a source to be resolved if the integrated flux of the fitted Gaussian is at least 2σ higher than the flux obtained from a point-source fit (see Tables 3.3 and 3.4). Note that for a point source the peak flux density equals the integrated flux. According to this definition, five of the detected sources (KG 49, WW Cha, HT Lup, IM Lup, RU Lup) are resolved by the ATCA, and three of the Lupus sources (IM Lup, RU Lup, HK Lup) are resolved by the SMA. In the case of KG 49 it is the envelope that is resolved, in the other cases the discs.

3.3.3 Opacity index

At low frequencies, i.e., in the Rayleigh-Jeans regime, the flux density, F_ν, is related to frequency, ν, by a power law: $F_\nu \propto \nu^\alpha$. One can determine the dust opacity index, β, where $\kappa_\nu \propto \nu^\beta$, from the observed spectral index, α, through

$$\beta \approx (\alpha - 2)(1 + \Delta), \tag{3.1}$$

where Δ is the ratio of optically thick to optically thin emission from the disc (Beckwith et al. 1990; Beckwith & Sargent 1991; Rodmann et al. 2006).

Due to the frequency dependence of the dust opacity, protoplanetary discs are generally optically thick at short wavelengths and optically thin at long wavelengths. Optically thick emission cannot be neglected in the inner disc where column densities get very high, even at very long wavelengths. The ratio of optically

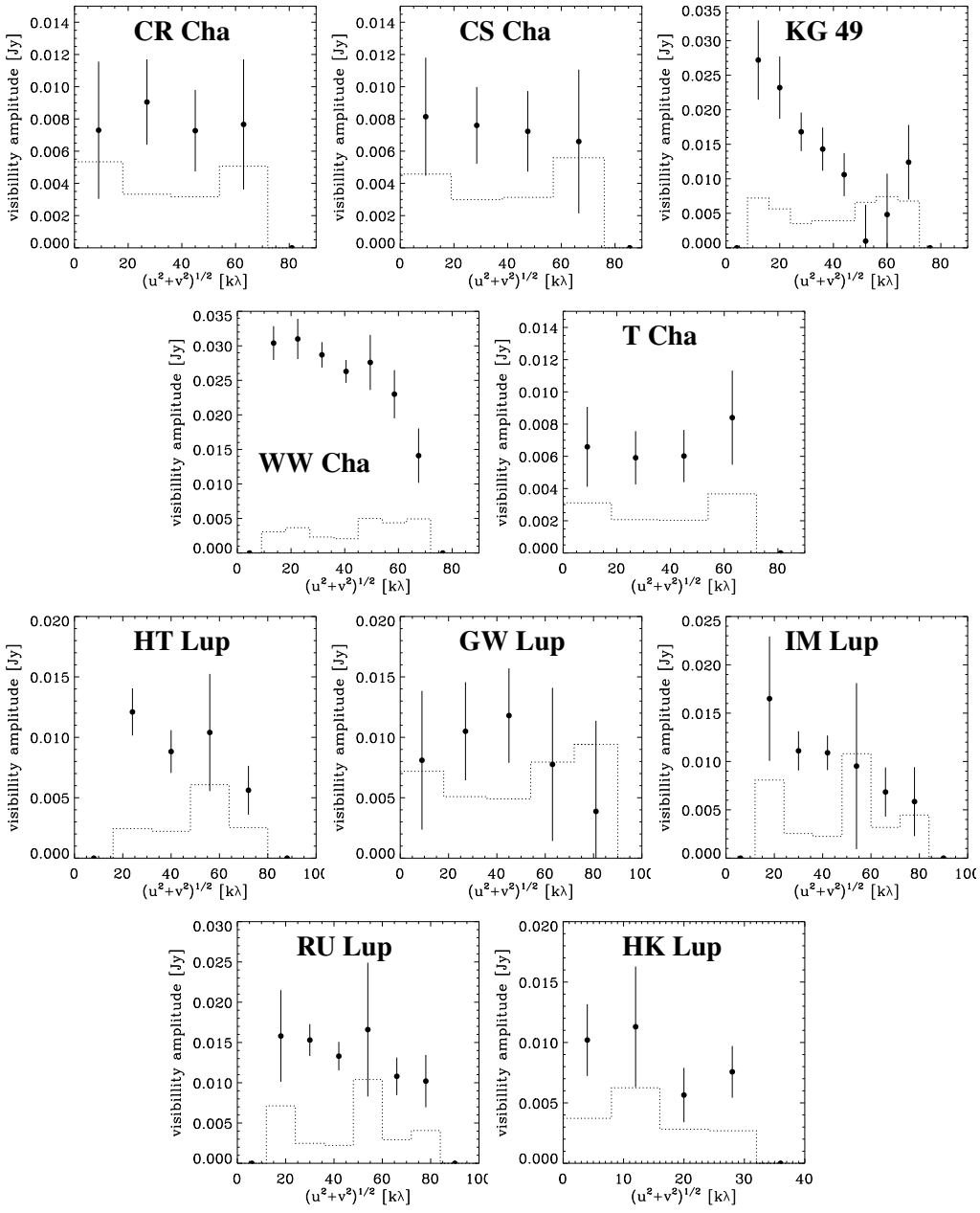

Figure 3.2: Amplitude vs (u, v) distance for sources observed with the ATCA. The data points give the vector-averaged amplitude per bin, where the data are binned in annuli according to (u, v) distance. The error bars show the statistical 1σ errors and the dotted lines give the expected amplitude for zero signal.

Table 3.5: SEST 1.3 mm fluxes from the literature, mm slopes, derived opacity indices, and disc masses.

Source name	SEST 1.3 mm[a] Flux (mJy)	Mm slope[b] α	Opacity index[b] β	Disc mass[c] $M_{\rm disc}$ ($M_\odot$)
SY Cha	< 172	...	...	< 0.011
CR Cha	125 ± 24	3.2 ± 0.5	1.5 ± 0.6	0.014
CS Cha	128 ± 46	2.9 ± 0.5	1.0 ± 0.6	0.021
DI Cha	38 ± 11	> 2.4	> 0.5	< 0.009
KG 28	...	...	...	< 0.009
Glass I	70 ± 22	> 3.4	> 1.7	< 0.007
WW Cha	408 ± 29	2.7 ± 0.7	0.8 ± 0.8	0.077
XX Cha	< 252	...	...	< 0.011
T Cha	105 ± 18	2.9 ± 0.5	1.1 ± 0.6	0.003
HT Lup	135 ± 15	2.5 ± 0.4	0.4 ± 0.5	0.025
GW Lup	106 ± 18	2.4 ± 0.4	0.5 ± 0.5	0.019
IM Lup	260 ± 9	3.2 ± 0.5	1.4 ± 0.5	0.027
RU Lup[c]	197 ± 7	2.5 ± 0.1	0.5 ± 0.1	0.032
HK Lup	84 ± 17	2.5 ± 0.4	0.7 ± 0.5	0.033

[a] Henning et al. (1993); Nürnberger et al. (1997).

[b] Calculated from SMA and ATCA fluxes (Gaussian fits) from this work and SEST fluxes, where available.

[c] Disc masses estimated from ATCA fluxes (Gaussian fits), assuming a gas-to-dust ratio $\Psi = 100$, a dust opacity at 3.3 mm $\kappa_\nu = 0.9$ cm^2 g^{-1}, and a dust temperature $T_{\rm dust} = 25$ K.

[d] Includes JCMT fluxes from Weintraub et al. (1989).

thick to optically thin emission coming from the disc is given by

$$\Delta \approx -p \times \left[(2-q)\ln\{(1-p/2)\bar{\tau}\}\right]^{-1}, \tag{3.2}$$

where p and q are the disc's surface density and temperature indices, and $\bar{\tau}$ is the average disc opacity at the frequency under consideration (see Beckwith et al. 1990, for details). Following Beckwith et al. (1990) and Rodmann et al. (2006), we used $p = 1.5$. q is uniquely determined from the spectral index at wavelengths where the dust opacity is high ($\lambda \leq 100\mu$m), and from IRAS photometry we obtained values ranging from 0.4 to 0.7. $\bar{\tau}$ can in principle only be determined if

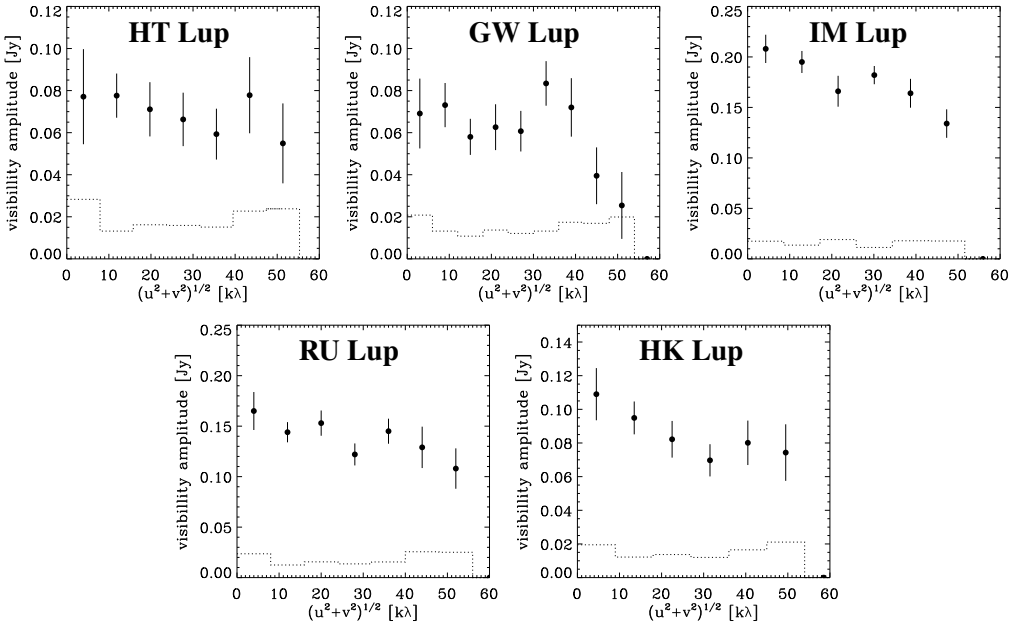

Figure 3.3: Same as Fig. 3.2 for sources observed with the SMA.

the physical disc radius is known. Rodmann et al. (2006) use $\bar{\tau} = 0.01$ at 7 mm. Taking $\beta = 1$ as a fiducial value for the opacity index, we adopt $\bar{\tau} = 0.02$ at 3.3 mm and find values for Δ ranging from 0.18 to 0.22.

The spectral index α and the opacity index β were determined from the ATCA 3.3 mm fluxes and SEST 1.3 mm fluxes from the literature (Nürnberger et al. 1997; Henning et al. 1993). The uncertainties in α and β are typically 0.5, due to both the large uncertainties in the absolute fluxes of the data points and to the relatively short wavelength range over which α was determined. For the Lupus sources, α was also determined with the SMA 1.4-mm fluxes included, giving consistent results. The robustness of the value for α is illustrated by Fig. 3.4, which shows the integrated fluxes from this work and single-dish (sub)millimetre fluxes from the literature for RU Lup (Weintraub et al. 1989; Nürnberger et al. 1997), along with the fitted slope: $\alpha = 2.5 \pm 0.1$. We thus find that the formal uncertainties in α and β for the other sources are probably overestimates. Unfortunately, RU Lup is the only source for which currently observations at such short wavelengths are available. The low error in the fit to its data point illustrates that more observations, preferably over a larger wavelength regime, will help to better constrain values for

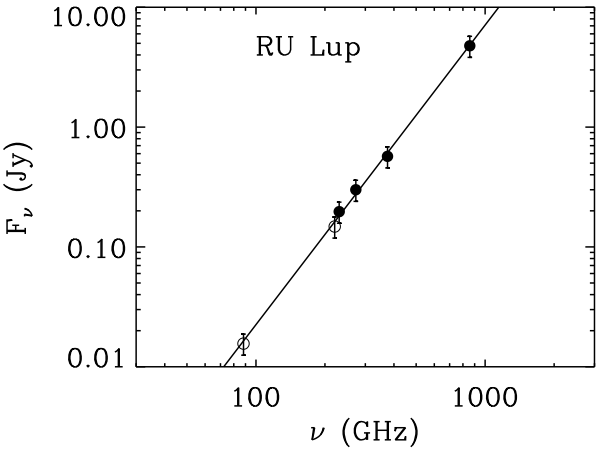

Figure 3.4: F_ν vs ν for RU Lup. Filled symbols show fluxes from single-dish observations (JCMT and SEST, Weintraub et al. 1989; Nürnberger et al. 1997), open symbols show the values for the interferometric observations from this work. All points fall on a line with $\alpha = 2.5 \pm 0.1$, where $F_\nu \propto \nu^\alpha$. This suggests that there is no extended emission over the size scale of the primary beams of the different telescopes, as may be the result of, e.g., a remnant envelope or ambient cloud material. Hence, no extended emission is filtered out in the interferometric observations.

α, and hence β.

The values for α and β for the sources in our sample are presented in Table 3.5. Fig. 3.5 shows the cumulative fraction of sources with given dust-opacity indices for our sample and that of Rodmann et al. (2006). Rodmann et al. corrected for the contribution of free-free radiation at 7 mm. We estimate the contribution of free-free radiation to be $\sim 5\%$ at 3.3 mm, and hence it is not necessary to correct for it at this wavelength. Fig. 3.4 illustrates that contamination from free-free emission is not an issue for RU Lup. The Kolmogorov-Smirnov test gives a probability of 58% that Rodmann et al.'s and our groups are drawn from the same distribution. However, the uncertainties in β are still quite large, and are not taken into account by the standard Kolmogorov-Smirnov test.

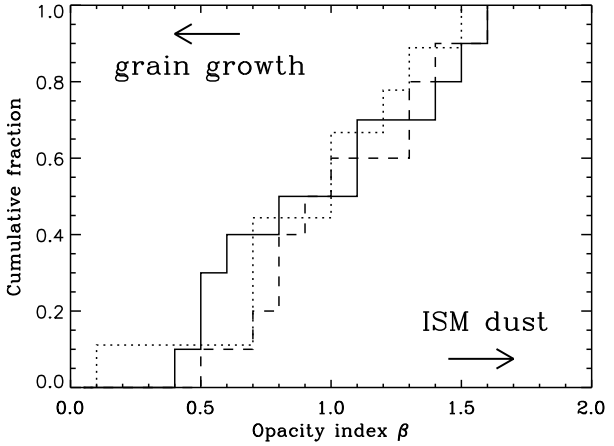

Figure 3.5: Cumulative number of sources with an opacity index less than a given value of β for the sources in our sample (solid line), those studied by Rodmann et al. (2006) (dashed line), and those studied by Natta et al. (2004) (dotted line).

3.3.4 Disc masses

For optically thin discs, the disc mass $M_{\rm disc}$ is directly proportianal to the flux F_ν (see, e.g., Hildebrand 1983; Natta et al. 2000):

$$M_{\rm disc} = \frac{F_\nu \Psi D^2}{\kappa_\nu B_\nu(T_{\rm dust})}, \tag{3.3}$$

where Ψ is the gas-to-dust ratio, D is the distance to the source, κ_ν is the dust opacity, and $B_\nu(T_{\rm dust})$ is the brightness at the frequency ν for a dust temperature $T_{\rm dust}$, as given by the Planck function. We used the integrated fluxes from the Gaussian fits, and assumed $\Psi = 100$, $T_{\rm dust} = 25$ K, and $\kappa_\nu = 0.9$ cm^2 g^{-1} at 3.3 mm [cf. Beckwith et al. (1990)[3]]. The derived disc masses for our sources range from < 0.01 up to 0.08 $M_\odot$, and are presented in Table 3.5. Note that the mass estimates are quite uncertain and may easily be off by a factor of 2, due to the uncertainties in the parameter values. Given the uncertainties in the measured quantities it is not meaningful to extend the analysis to include the contribution of optically thick emission and detailed disc structure.

[3]Note that Beckwith et al. (1990) estimate $\kappa_\nu = 0.1(\nu/10^{12}\ {\rm Hz})^\beta$ cm^2 g^{-1}, where κ_ν is the opacity index *for the gas and the dust combined*, i.e., with an implied gas-to-dust ratio. Our values for κ_ν, however, are for the dust alone, and hence we have to account for the gas-to-dust ratio explicitly.

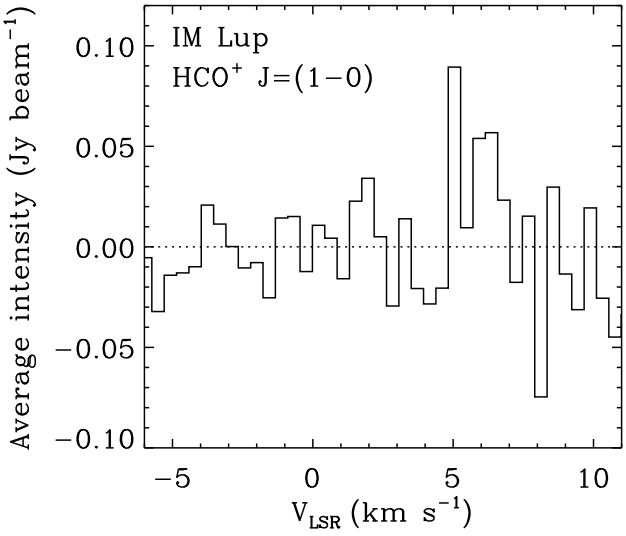

Figure 3.6: Spectrum of HCO^+ J = 1–0 line emission observed from IM Lup, at the position of the peak continuum emission, binned to 0.44 km s^{-1} velocity resolution, in the 2.″3 × 1.″7 synthesised beam.

3.3.5 Molecular line emission

Both IM Lup and WW Cha were observed in spectral-line mode to search for HCO^+ J = 1–0 emission. In general, CO is a more easily detectable gas tracer in the millimetre regime, but since the ATCA does not presently have the capability to observe at frequencies above 106 GHz, HCO^+ was used to investigate the gas component of discs. We tentatively detect HCO^+ at $\sim$ 0.05 Jy beam^{-1} in IM Lup, as presented in Fig. 3.6. Van Kempen et al. (2006) detected a double-peaked feature, consistent with a rotating gas disc, using JCMT observations of the ^{12}CO J = 3–2 line. However, they find the line at $\sim$1 km s^{-1} lower velocity. The cause of this discrepancy is unclear.

A ray-tracing programme (Hogerheijde & van der Tak 2000) was used to compute the line profile of HCO^+ J = 1–0, using the model for IM Lup described in van Kempen et al. (2007). The abundance of HCO^+ was set to be 10^{-8} with respect to H_2 in areas with temperatures above 30 K, and 10^{-12} in areas with temperatures below 30 K. An intensity of $\sim$ 0.02 Jy beam^{-1} was predicted, consistent with the observations within the uncertainties.

No HCO^+ line emission is detected to a limit of 97 mJy beam^{-1} (3σ) in the direction of WW Cha. Combining our new results with those of Wilner et al. (2003) who detected HCO^+ in TW Hya, but not in HD 100546, we have two detections of HCO^+ and two non-detections. Data for more targets are required, in order to determine whether the presence of HCO^+ is related to the disc's evolutionary state.

3.4 Discussion and interpretations

3.4.1 Grain growth

About half the sources that are detected are spatially resolved. The inferred physical sizes (disc radii of $\sim$ 100 AU) indicate that the emission coming from the discs is predominantly optically thin at millimetre wavelengths. This is illustrated by the work of Testi et al. (2001), who do detailed modeling of the Herbig-Ae stars UX Ori and CQ Tau, and find that disc radii of $\sim$ 100 AU, combined with millimetre slopes of $\lesssim 3$ and 1.3 mm fluxes of $\sim 10^2$ mJy, are well explained by an opacity index $\beta = 1.0$. If we assume that all sources in our sample are optically thin at millimetre wavelengths, the opacity index β can be determined. Seven out of ten detected sources have $\beta \lesssim 1$, which can be naturally explained by grain growth to millimetre and centimetre sizes (Draine 2006).

3.4.2 Comparison with Spitzer infrared data

Our values for β indicate grain growth to sizes of millimetres and larger in the outer discs. The surface layers of the inner discs can be probed by infrared observations and, as noted in Sect. 3.1, the 10-μm feature indicates the growth of grains through changes in its strength and shape.

In Fig. 3.7 we compare the millimetre slope α as derived in Sect. 3.3 with the "strength" or peak 10-μm flux ($S_{\rm peak}^{10\mu{\rm m}}$) and to the "shape" or the ratio of the 11.3 to 9.8 μm flux ($S_{11.3}/S_{9.8}$) of the 10-μm silicate feature for those sources in our sample that overlap with the samples of Przygodda et al. (2003) and Kessler-Silacci et al. (2006). Here the normalized 10-μm spectra S_ν are given by

$$S_\nu = 1 + \frac{(F_\nu - F_{\nu,c})}{< F_{\nu,c} >}, \tag{3.4}$$

where F_ν is the observed spectrum and $F_{\nu,c}$ is the fitted continuum, and $< F_{\nu,c} >$ is the frequency-averaged continuum flux (see Kessler-Silacci et al. 2006 for details). We find a positive correlation between α and $S_{\rm peak}^{10\mu{\rm m}}$ and a negative cor-

relation between α and $S_{11.3}/S_{9.8}$, especially if we leave out the source T Cha, which shows emission from polycyclic aromatic hydrocarbons at 11.3 μm and may be considerably older than the other sources in the sample. As grains grow from submicron sizes to several microns, the 10-μm feature becomes weaker and less peaked (see, e.g., Kessler-Silacci et al. 2006), and thus the correlations we find may well indicate that once grain growth starts, the grains quickly grow from (sub)micron sizes to millimetre sizes and larger, both in the inner and outer discs. This is consistent with grain-growth models (Weidenschilling 1988, 1997; Dullemond & Dominik 2004b, 2005), which show that growth to metre sizes is rapid ($\sim 10^3$ yr at 1 AU; $\sim 10^5$ yr at 30 AU).

On the other hand, while a significant fraction of the dust has already grown to sizes of millimetres and centimetres, the infrared data indicate that micron-sized grains are also still present, at least in the surface layers. This may be explained by assuming that not only grain growth, but also aggregate fragmentation takes place in the discs (Dullemond & Dominik 2005). After about 10^4 years a semi-stationary state is reached for sizes below $a \lesssim 1$ cm, which may last for several 10^6 years.

Note that Fig. 3.7 shows a trend rather than a bimodal distribution. Dullemond & Dominik (2005) suggest fragmentation of grains to allow for the semi-stationary state that is observed in the discs around T-Tauri stars. If the correlation between the 10-μm feature and the millimetre slope is confirmed by a more extensive dataset, it would indicate that when aggregates are fragmented in collisions, the size of the fragments increases as the aggregate sizes increase. Hence, when the largest particles grow from millimetre to centimetre sizes, the submicron-sized grains are no longer replenished, and the 10-μm feature – tracing the upper layers of the disc where the stirred-up small particles reside – flattens while the millimetre slope – which traces the midplane where the largest particles are present – becomes shallower.

We also compared α to the spectral index over the 13 to 35 μm range from Kessler-Silacci et al. (2006). However, α could only be determined for five of the sources in Kessler-Silacci et al., and no obvious correlation is found for this small sample.

3.4.3 Comparison with Herbig-Ae/Be stars

It is interesting to note that Acke & van den Ancker (2004) do *not* find a correlation between the 10-μm silicate feature and the (sub)millimetre spectral index for their sample of 26 Herbig-Ae/Be stars. On the other hand, Acke et al. (2004) *do* find a correlation between the shape of the mid-IR (12–60 μm) SED and the

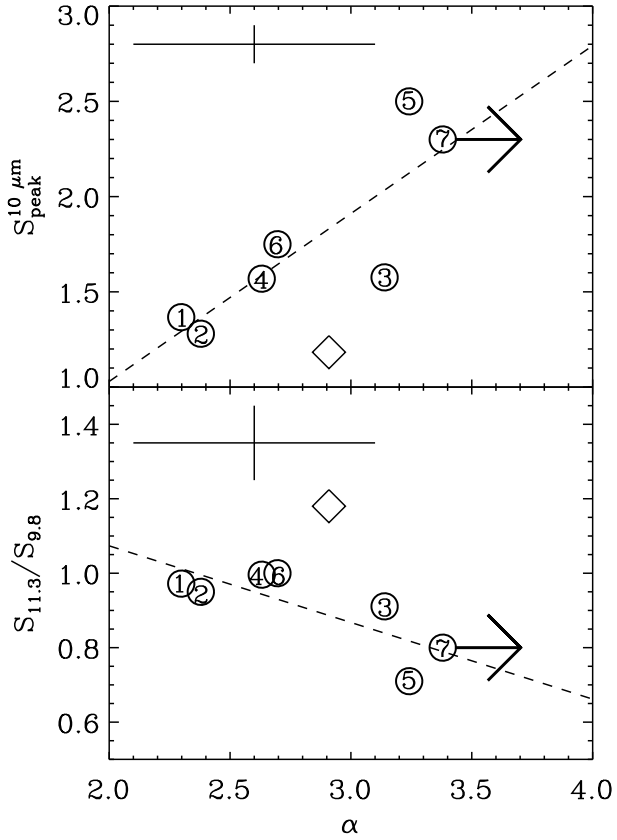

Figure 3.7: Slope in the millimetre regime vs the peak 10-μm flux (upper panel) and the ratio of the 11.3 to 9.8 μm flux (lower panel) of the 10-μm silicate feature, for those sources in our sample for which data are available. 1=HT Lup, 2=GW Lup, 3=IM Lup, 4=RU Lup, 5=CR Cha, 6=WW Cha, 7=Glass I. The source T Cha is depicted with a diamond.

(sub)millimetre slope in their sample. They interpret this finding as a correlation between disc geometry and grain size: as grains grow, the disc structure evolves from flared to geometrically flat (see, e.g., Dullemond 2002). For the twelve sources in our sample for which it was possible to determine α, we determined the non-colour-corrected *IRAS* [12]–[60] colour and compared this to α. No clear correlation was found, consistent with the above lack of correlation with

the 13–35 μm spectral index. This may indicate that grain growth has a less dramatic effect on the geometry of discs around the low-mass T-Tauri stars than on the intermediate-mass Herbig-Ae/Be stars, or that *IRAS* fluxes are contaminated by other (extended) emission in the large *IRAS* beams.

Natta et al. (2004) did a study similar to ours for a sample of six isolated Herbig-Ae stars and three T-Tauri stars. They estimated β in two different ways, firstly using only interferometric data, and secondly with single-dish data included. Their results are included in Fig. 3.5, where the values for β with the single-dish data included were used for comparison. According to the Kolmogorov-Smirnov test there is a 65% probability that the sample of Natta et al. and our sample are drawn from the same distribution. It is interesting to note that in general the sources in Natta et al.'s sample are considerably older than those sources in the current work and that of Rodmann et al. (2006). This may be an extra indication that the size distribution of grains in protoplanetary discs remains stationary for several Myr once sizes of millimetres are reached.

3.5 Concluding remarks

We used the ATCA to make interferometric observations of fifteen southern T-Tauri sources at 3.3 mm. Ten of the sources are located in Chamaeleon, the remaining five in Lupus. The Lupus sources were also observed at 1.4 mm with the SMA. The main results are as follows.

- Five of the Chamaeleon sources were detected at the 3σ level or better with the ATCA, for the other five sources we have strict upper limits.
- All five Lupus sources were detected at better than 3σ with the ATCA, and at better than 15σ with the SMA.
- Five of the ten detected sources are spatially resolved with the ATCA, and two of the five Lupus sources are resolved with the SMA. This indicates that the emission coming from these sources is optically thin.
- Adopting optically thin emission for all sources in our sample, we estimated the opacity index β. We find that $\beta \lesssim 1$ for seven of the ten detected sources. Such values for β can be naturally explained by grain growth up to millimetre sizes and beyond.
- We find a tentative correlation between the millimetre slope and the peak 10-μm flux and ratio of the 11.3 to 9.8 μm flux of the 10-μm silicate feature. This indicates that grain growth takes place in the outer disc and in the

surface layers of the inner disc simultaneously. It also confirms earlier findings that agglomerate destruction must take place in the disc to preserve the small grain population. If confirmed by more extensive datasets, this correlation may be an indication that larger aggregates produce larger particles when fragmented in collisions.

- HCO^+ was tentatively detected in IM Lup, and was not seen in WW Cha.

This type of work will be greatly assisted by the upcoming 7 mm upgrade for the ATCA, as well as by the installation of a new correlator via the Compact Array Broadband Backend project. Estimating the millimetre slope over a wavelength range up to 7 mm will reduce the error in α – and hence in β – from ~ 0.5 to ~ 0.2. At these longer wavelengths, however, the contribution of free-free emission becomes important, and lower-frequency measurements are required to separate the various contributions. A pilot study to determine the contribution of free-free emission at centimetre wavelengths in our sources is in progress.

The capability to observe the continuum across a 2 GHz bandwidth, as opposed to the current 128 MHz, will provide a marked increase in sensitivity, allowing more discs to be detected. Furthermore, as the new generation of (sub)millimetre interferometers, notably eSMA, CARMA, and ALMA, becomes available to the scientific community, it becomes possible to resolve the circumstellar discs at millimetre and submillimetre wavelengths down to subarcsecond scales. A survey of a large sample of objects, in different clouds, and at higher resolution will greatly enhance our understanding of the timescale for grain growth and the building of planetary systems as a function of disc radius.

Acknowledgements

We would like to thank the ATNF for their hospitality and assistance, and specifically Tony Wong for extensive assistance during the observations and the data reduction. SMA staff, in particular Alison Peck, are thanked for scheduling observations of the Lupus sources as a filler programme and for carrying out the observations. Partial support for this work was provided by a Netherlands Research School For Astronomy network 2 grant, and by an Netherlands Organisation for Scientific Research Spinoza grant. CMW acknowledges financial support from an ARC Australian Research Fellowship. We are grateful to Jackie Kessler-Silacci for providing us with infrared data, and to Tim van Kempen for useful discussions on IM Lup and calculating the HCO^+ emission in his model. Finally, we would like to thank our referee, Claire Chandler, for useful comments that significantly improved this paper.